This is a post-peer-review, pre-copyedit version of an article published in Experiments in Fluids. The final authenticated version is available online at: https://doi.org/10.1007/s00348-021-03308-2
Experiments in Fluids (2021) 62:216

Nucleation and cavitation number effects on tip vortex cavitation dynamics and noise

M.T. Khoo · J.A. Venning · B.W. Pearce · P.A. Brandner

Abstract
The spatial and acoustic characteristics of tip vortex cavitation (TVC) inception were measured in a cavitation tunnel. Numerous cavitation events were recorded to reveal the influence of different nuclei populations and cavitation numbers on nuclei capture and activation physics, and the role of the streamwise pressure distribution in a vortex. Synchronised high-speed video and hydrophone measurements of cavitation events were taken in the trailing vortex of an elliptical hydrofoil at an incidence of 6° and a Reynolds number of 1.5×10^6. The injected nuclei population in the tunnel test section was varied by using different microbubble generators mounted upstream of the test section. Both the nuclei population and cavitation number have a significant effect on the inception location distribution along the trailing vortex, and in particular, inception event rates. The cavitation number alters the flow volume subjected to tension, thereby also affecting the shape of the inception location distribution. Once the nuclei are activated, cavity kinematic and acoustic properties are influenced by the local pressure (i.e. inception location and cavitation number) more so than initial nucleus size, at least in the ∼50–100 µm diameter range considered in this study. Inception events that occur near the tip generate stronger acoustic pulses. At these inception locations, the frequency of the tonal peak associated with inception remains relatively constant for the two nuclei populations, but increases with cavitation number. This study provides insights into the roles of nucleation and cavitation number in TVC, and informs future measurements and predictions of TVC dynamics and noise.

Keywords Tip vortex cavitation · Nuclei · Cavity dynamics · Cavity acoustics

M.T. Khoo
Maritime Division
Defence Science and Technology Group
Melbourne, Australia
E-mail: matthew.khoo@dst.defence.gov.au

M.T. Khoo · J.A. Venning · B.W. Pearce · P.A. Brandner
Cavitation Research Laboratory
University of Tasmania, Launceston, Australia

1 Introduction

Cavitation inception in practical flows is typically heterogeneous in nature and occurs when a nucleus, such as a microbubble, is exposed to its size-dependent critical pressure, resulting in explosive growth. The vortex trailing from a three-dimensional lifting surface is characterised by a low-pressure core in which cavitation is most likely to appear (see Fig 1). Nuclei within its streamtube may be activated, as well as nuclei drawn into the vortex by its radial pressure gradient. This phenomenon is known as tip vortex cavitation (TVC). It is often the first type of cavitation to occur about marine propellers and is detrimental to acoustic stealth performance.

Nuclei populations are known to vary within and between environmental and laboratory waters (Khoo et al., 2020c). They can influence TVC inception behaviour, with the earlier onset of cavitation measured in flows with higher concentrations of larger nuclei, also known as ‘weak’ water, as opposed to ‘strong’ water devoid of nuclei (Arndt and Keller, 1992; Gindroz and Billet, 1998; Khoo et al., 2018). Numerical simulations of TVC in flows with different nuclei populations have shown that fewer nuclei activations occur for populations with smaller nuclei (Hsiao and Chahine, 2005). In nature, these populations vary with location and depth (Gindroz et al., 1995; Gowing and Shen, 2001), as well as sea state (Johnson, 1986) and potentially biological activity (O’Hern et al., 1986). During experimental studies of TVC in cavitation tunnels, nuclei populations have been controlled by manipulation of the dissolved air content (Arndt and Maines, 2000; Chang et al., 2011) and by microbubble injection into the test flow (Briançon-Marjollet and Merle, 1996; Peng et al., 2017), the latter enabling more independent control over free and dissolved gas and thus their effects on cavitation behaviour. Nuclei populations have size and concentration distributions (Khoo et al., 2020c; Russell et al., 2020b), as well as spatial distributions. The arrival of a nucleus at a particular location, the low pressure vortex core in this case, is stochastic in nature. Therefore TVC inception is a stochastic process and large datasets may be required for accurate characterisation. For a flow deplete of nuclei, Khoo et al. (2020b) found that some hundreds of events are required to characterise the probability of TVC inception in a trailing vortex subjected to a given tension due to variability in the waiting time associated with nuclei capture. A flow abundant with nuclei is expected to require short waiting times with less variability.

The cavitation number is a non-dimensional quantity which controls the likelihood and scale of cavitation in a flow. In natural environments, it varies with the operational depth and velocity of the component, as well as the properties of the liquid. In cavitation tunnels, it is typically set via tunnel pressure or flow velocity, or some combination of the pair. Maines and Arndt (1993) investigated TVC about an elliptical hydrofoil, and found that at higher cavitation numbers, TVC appears as unsteady, isolated events. A reduction in the cavitation number results in the development of

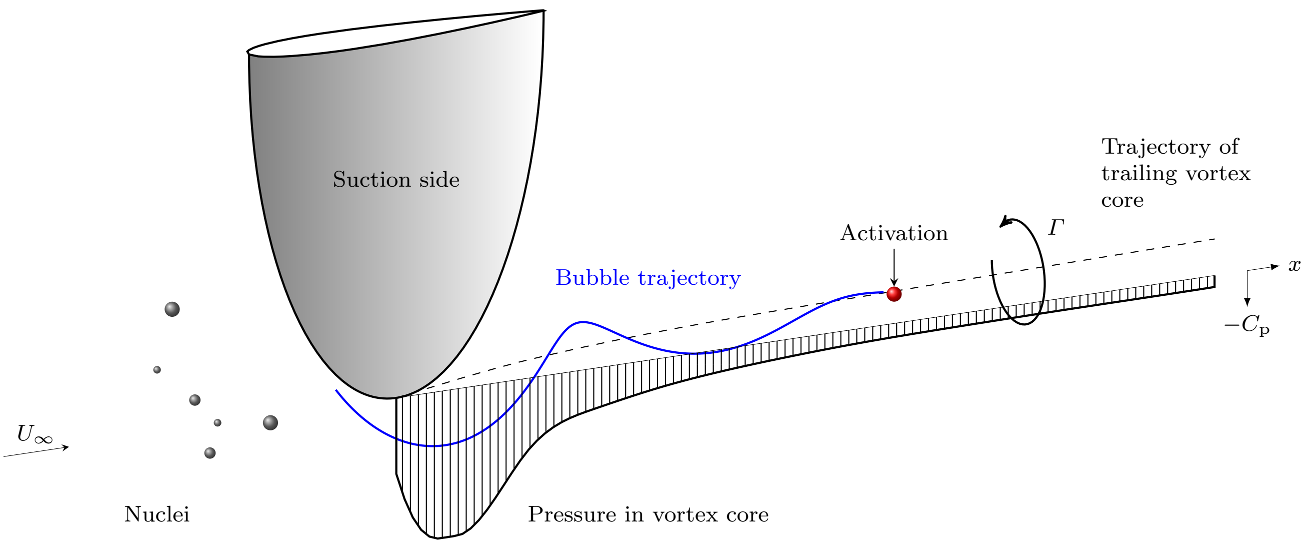

Fig. 1 Notional capture of a nucleus (red sphere) into the vortex trailing from a lifting surface. The blue line denotes the nucleus trajectory. The freestream velocity is U_∞ and the circulation is Γ. The generic variation of the pressure coefficient, C_p, with streamwise location, x, similar to the trends observed for elliptical foils (Chen et al., 2019; Asnaghi et al., 2020), is also shown with the minimum pressure occurring close to the tip and pressure recovery downstream as the vortex diffuses.

a fully-cavitating vortex core with a characteristic bulbous head at the upstream extent of the cavity. This cavity moves upstream and attaches to the tip at even lower cavitation numbers. The appearance of TVC at inception is also dependent on the nuclei population. In strong water, TVC does not appear until high tensions are applied, in which case it manifests as a steady cavity, rather than isolated events (Khoo et al., 2018).

TVC inception location is of interest because the streamwise pressure distribution may affect tip vortex cavity dynamics and acoustics. The pressure distribution within a tip vortex, and hence the location of minimum pressure, close to the tip is dependent on hydrofoil planform, cross-section and tip geometry (Astolfi et al., 1999). The location of minimum pressure has been measured to be between 0.075 and 0.125 chord lengths downstream of the tip for elliptical hydrofoils in experimental (Fruman and Dugue, 1994) and numerical (Hsiao and Chahine, 2005; Asnaghi et al., 2020) studies. Cavitation inception may occur at streamwise locations along the vortex away from the location of minimum pressure, as long as the local pressure is sufficiently low to activate a captured nucleus. The capture of a nucleus is dependent on vortex strength, bubble size and its distance from the vortex (Ligneul and Latorre, 1989, 1993; Chen et al., 2019).

Quantitative data on TVC inception location is scarce. Anecdotal observations indicate that inception usually happens near the tip in weak water (Maines and Arndt, 1993; Arndt and Maines, 2000), but can occur between −0.05 and about 1.5 chord lengths downstream of the tip (Maines and Arndt, 1993; Higuchi et al., 1989). Arndt and Maines (2000) reported that in strong water, inception is equally likely between 0.05 and 1.0 chord length downstream of the tip, but quantitative distributions were not provided. In contrast, a more uniform distribution of inception locations was observed in a weaker flow seeded with larger monodisperse bubbles, compared to a stronger flow with a polydisperse distribution of smaller bubbles (Khoo et al., 2020a). In that study, the water quality was controlled by varying the free gas content (i.e. the nuclei population), rather than the dissolved or total gas content as done by Arndt and Maines (2000). More detailed studies are required to characterise nucleation and cavitation number effects on TVC inception location distribution, with a view to understanding cavity dynamics and acoustics.

A number of studies on TVC bubble dynamics can be found in the literature. Inception was observed to comprise of four phases by Maines and Arndt (1993):

1. Spherical nucleus entrainment.
2. Spheroidal bubble growth.
3. Transitional phase.
4. Cylindrical bubble growth.

Spheroidal growth is followed by axial stretching, with the cavity observed to initially elongate at a relatively constant rate. The elongation rate, which has been found to vary between one and almost five times the freestream velocity, is dependent on nucleus capture location and is higher when entrainment occurs closer to the tip (Arndt and Maines, 2000). For lower elongation rates, the cavity grows as it is advected downstream, but for higher elongation rates, the head of the cavity remains stationary as the tail extends downstream. The elongation rate decreases downstream in the pressure recovery region (Choi and Ceccio, 2007). A relationship between the elongation rate and theoretical vortex tension was proposed by Arndt and Maines (2000), but poor correlation was observed, suggesting the need for more detailed analytical models. High speed video measurements of TVC in a flow saturated with air showed that the maximum cavity elongation rate occurs when the bubble centre is between approximately 0.2 and 0.25 chord lengths downstream of the tip, although a significant degree of scatter was present in the dataset (Maines and Arndt, 1993). Based on the complexity of tip vortex cavity development from nucleus capture to cylindrical cavity elongation, Maines and Arndt (1993) concluded that spherical bubble dynamics do not adequately describe inception.

The theory of bubble acoustics has been studied in depth. The acoustic pressure generated by a bubble is dependent on its radius and the first and second time derivatives of the radius, and therefore its volumetric acceleration (Lamb, 1945; Fitzpatrick, 1958; Leighton, 2012). The natural frequency of spherical bubble oscillation was initially derived by Minnaert (1933), then extended by others, including Brennen (1995), to account for surface tension. Larger bubble radii and lower external pressures result in lower resonant frequencies. This is similar to the resonant frequencies of cylindrical cavities given by Neppiras (1980), for which longer cavities resonate at lower frequencies.

Some observations of water quality effects on tip vortex cavity dynamics and noise can be found in the literature. Higher cavity elongation rates have been observed in flows with stronger nuclei (Arndt and Maines, 2000), although these results may also be affected by the different tensions in the vortex required to activate nuclei with different critical pressures, which complicates the analysis. Choi et al. (2009) found numerically that larger nuclei with critical pressures close to vapour pressure grow in a quasi-steady manner subjected to slowly-applied tension, while nuclei under high tension grow explosively to a diameter larger than the equilibrium diameter before oscillating and generating noise. By varying the nuclei size distribution, Hsiao and Chahine (2005) observed fewer acoustic pressure pulses in flows with stronger, smaller nuclei. Although similar trends in acoustic magnitude were measured in strong and weak flows during the onset and development of TVC, higher sound pressure levels and different cavity appearances were observed for the latter (Khoo et al., 2018). The experiments of Higuchi et al. (1989) suggest that dissolved gas content does not influence TVC acoustics. Moreover, the cavitation number was found to have a moderate effect on simulated peak pressures of microbubbles during initial growth (Choi and Chahine, 2003). Depending on the bubble model employed, the highest acoustic pressures occurred during bubble collapse (spherical model) or splitting (non-spherical model), rather than initial growth. Hsiao and Chahine (2005) showed numerically that bubble collapse noise increases in magnitude with decreasing cavitation number.

It is evident that the nuclei population, along with the pressure field, control TVC inception. While numerous studies have been carried out into TVC kinematics and acoustics, there is a lack of experimental studies on nucleation and cavitation number effects using strictly controlled nuclei populations. To quantify the influence of nucleation and cavitation number on TVC behaviour and its associated physics, the spatial and acoustic characteristics of hydrofoil TVC were studied in a cavitation tunnel, and related to inception locations along the vortex. Synchronised high speed video and acoustics measurements of $\mathcal{O}(1000)$ intermittent cavitation events were made. Nucleation effects were studied by varying the microbubble population in the tunnel test section. The influence of cavitation number was also investigated by changing the test section static pressure. This work provides greater insight into the effect of the vortex streamwise pressure distribution on nuclei capture and TVC development. Indeed for the monodisperse case discussed later, this pressure distribution can be inferred from the distribution of inception locations. Further insights are also gained into the importance of nuclei content and cavitation number for the measurement and prediction of TVC dynamics and noise.

2 Experimental overview

2.1 Test facility

The cavitation tunnel in the Australian Maritime College (AMC) Cavitation Research Laboratory is located in Launceston, Australia. It is a medium-sized, variable pressure water tunnel constructed of stainless steel (wetted areas). The tunnel volume is 365 m^3 and the working fluid is demineralised water. The test section cross section measures 0.6 m × 0.6 m, with a length of 2.6 m. The test section pressure, p_∞, can be varied between 4–400 kPa absolute, while the test section velocity, U_∞, range is nominally 2–12 m/s.

The tunnel design and ancillaries enable strict control over both free and dissolved gas contents. Millimetre-sized bubbles are removed in a large tank downstream of the test section via coalescence and gravity separation. Smaller bubbles dissolve in the lower segment resorber due to extended residence at high static pressure. This avoids the recirculation of free gas bubbles that are either injected or generated by cavitation about a test component. The tunnel also features a fast degassing facility, by which the dissolved gas content can be reduced. Further details on the facility are provided in Brandner et al. (2007).

2.2 Experimental setup

The stainless steel hydrofoil used for this study has an elliptical planform and a NACA 0012 cross section. The root chord length is 150 mm and the span is 300 mm. The hydrofoil was mounted to the test section ceiling, 1.45 m from the test section entrance, as shown in Fig. 2. The incidence was set to 6°.

Optical measurements were acquired with a Phantom v2640 high speed camera mounted beneath the test section. A 24 mm Nikkor lens was used, providing a magnification of 3.57 pixels/mm. Images were acquired at 2048 × 200 pixels (574 × 56 mm) at a frame rate of 16,000 fps. Constellation LED lights were used for illumination. Acoustic measurements were taken using a hydrophone (Brüel & Kjær Type 8103, sample rate 200 kHz) mounted in a side window at test section mid-height, 0.2 chord lengths downstream of the hydrofoil tip. Details of the hydrophone mounting arrangement can be found in Doolan et al. (2013). The hydrophone signal was conditioned using a Brüel & Kjær Type 2692-A charge amplifier and recorded using a 24-bit data acquisition card (National Instruments PXIe-4497).

Nucleation effects on TVC inception behaviour were investigated using two injected nuclei populations. An injected monodisperse microbubble population (hereinafter termed 'monodisperse') with a dominant bubble diameter of 91 µm in the test section was generated using a stainless steel 'T'-junction with 100 µm bore from Valco Instruments Co. Inc.. This is based on a device designed by YLec Consultants as described in Russell et al. (2018). A single nuclei generator was mounted upstream of the contraction, at the mid-span and mid-height of the plenum, as shown in Fig. 2.

An injected polydisperse microbubble population (hereinafter termed 'polydisperse') featuring bubbles with a range of diameters was also used. These microbubbles are generated in devices via the depressurisation of supersaturated water (Giosio et al., 2016). An array of these devices is mounted in the plenum (Russell et al., 2020b). They are typically arranged in a triangular grid, 80 mm apart (an equivalent spacing of 30 mm in the test section), mounted across three columns of a supporting strut. In the present study, a lower concentration of polydisperse nuclei was generated by only using the two outer columns. This results in spanwise and vertical spacing between generators of 139 and 80 mm, respectively.

The mono- and polydisperse nuclei generators each produce a plume with a diameter of about 80 mm in the test section. Each plume is presumed to have a spatial concentration profile that follows a Gaussian distribution due to turbulent mixing in the plenum. The monodisperse plume and the centre of four overlapping plumes generated by the polydisperse array were observed to be centred on the foil tip. The close spacing of the polydisperse generators relative to the plume size resulted in a near homogenous distribution within the nuclei capture streamtube which is $\mathcal{O}(10)$ mm in diameter.

An optical measurement technique called Mie scattering imaging (MSI) was used to quantify the injected nuclei populations within the test section (Russell et al., 2020a,b). Measurements were taken $2.2c$ upstream of the hydrofoil tip such that the measured populations were representative of those captured by the vortex. Microbubbles were illuminated with a 532 nm laser (Ekspla, Lithuania) and defocussed photographs were acquired using a 48 megapixel camera (IO Industries, Canada). Bubble diameters are calculated using the spatial frequency of the interference fringes in the defocussed images (Russell et al., 2020a,b).

2.3 Test conditions

Two types of tests were conducted. Firstly, a cavitation number, σ, of 1.6 was used to compare the effects of mono- and polydisperse nuclei populations on TVC inception dynamics and acoustics. The cavitation number is defined as $\sigma = \frac{p_\infty - p_\mathrm{v}}{q}$, where p_∞ is the freestream pressure upstream of the hydrofoil tip, p_v is the vapour pressure, $q = \frac{1}{2}\rho U_\infty^2$ is the freestream dynamic pressure and ρ is the fluid density. Secondly, cavitation number effects were studied by varying p_∞. A cavitation number range between 1.6 and 2.4 was investigated with the monodisperse population. For each type of test, synchronous optical and acoustic measurements were made in multiple 30.6 s blocks.

The Reynolds number, Re, was fixed at 1.5×10^6. It is defined as $Re = \frac{U_\infty c}{\nu}$, where c is the hydrofoil root chord length and ν is the kinematic viscosity of the water.

The polydisperse nuclei population was controlled by maintaining a constant generator cavitation number, σ_gen, of 0.7. This is defined as $\sigma_\mathrm{gen} = \frac{p_\mathrm{down} - p_\mathrm{v}}{p_\mathrm{up} - p_\mathrm{down}}$, where p_up is the pressure upstream of the generator orifice and p_down is the generator outlet pressure. The pressure upstream of the orifice was adjusted to maintain a constant generator cavitation number for the different test section conditions. For a cavitation number of 1.6, the monodisperse nuclei population was controlled by setting the inlet air and water pressures of the generator, as described in Russell et al. (2018). For the study of cavitation number effects, the inlet pressures were adjusted to maintain a constant pressure difference between the supply pressures and the plenum pressure at the outlet of the generator.

The two injected microbubble populations are shown in Fig. 3. Both cumulative and non-cumulative forms are provided. Measurements were acquired at the same nominal test section operating conditions as those used to study nucleation effects. The monodisperse and poly-

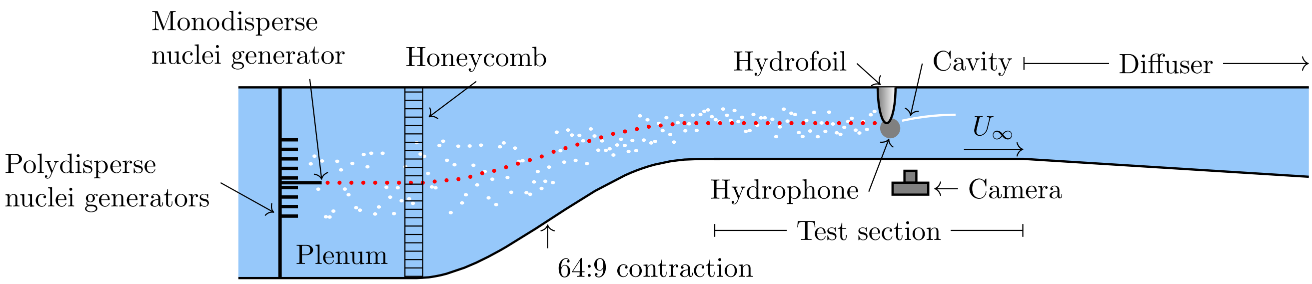

Fig. 2 Schematic of the experimental setup in the upper segment of the cavitation tunnel, showing the hydrofoil located in the test section. The test section velocity is U_∞. Mono- and polydisperse nuclei populations were injected upstream of the test section for different test runs. They are shown as red and white dots, respectively. The locations of the high speed video camera and hydrophone used for TVC inception observations are also denoted.

disperse nuclei distributions are constructed from 271 and 15 bubble detections, respectively. Larger sample sizes would be preferred, especially for the polydisperse population. However, very long acquisition times are required to measure lower bubble concentrations due to the relatively small field of view for MSI measurements. In this instance, an extrapolation of the measured nuclei distributions in Russell et al. (2020b) to higher generator cavitation numbers indicate that the polydisperse population measured in this study is reasonable and the sample size used is adequate.

The monodisperse population has a dominant bubble diameter of 91 µm. The critical pressure, p_c, of such bubbles is effectively vapour pressure (Khoo et al., 2020c). The polydisperse nuclei distribution features bubbles with a range of smaller diameters, in concentrations lower than that of the peak concentration for the monodisperse case. The diameter of the largest bubble detected was 88 µm, with a concentration more than two orders of magnitude less than for the monodisperse population. The total measured concentrations are similar between the mono- and polydisperse populations, at 5×10^3 and 4×10^3 m^{-3}, respectively.

The dissolved oxygen content was maintained between 1.9 and 4.0 mg/L (i.e. 21–45% relative to saturation at atmospheric pressure) throughout the experiment. The relative saturation level of dissolved oxygen in the water, r_{up}, using the plenum upstream of the test section as the reference location, was maintained between 13 and 27% during the present study which ensured that the natural nuclei population (i.e. the existing nuclei in the tunnel water without nuclei injection) remained at the baseline, as described in Khoo et al. (2020c). In flows with injected nuclei, the total population comprises of both the natural and injected nuclei. As shown in Fig. 3(a), the natural nuclei population is much stronger than the injected populations, and can be shown to be inactive during these experiments.

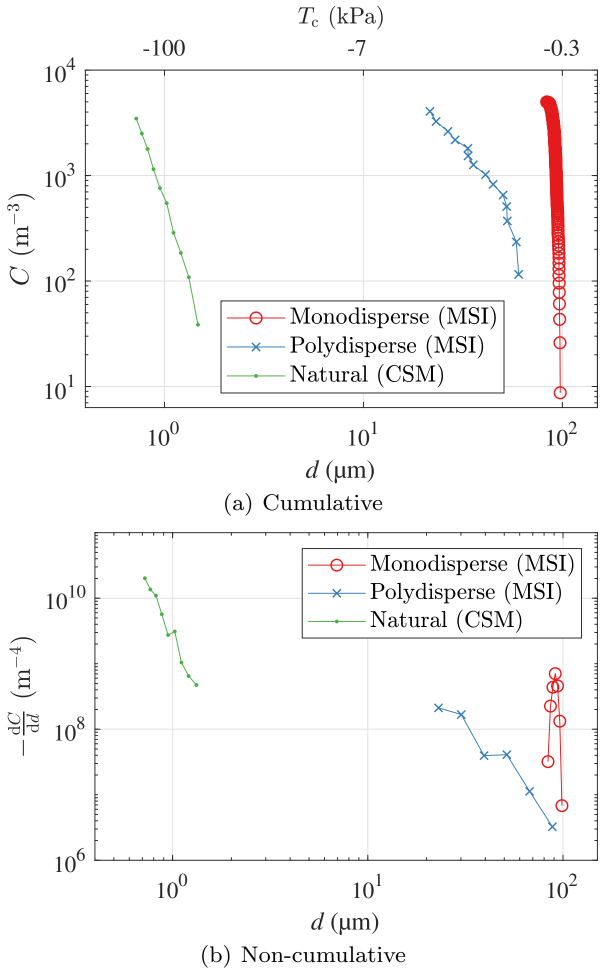

Fig. 3 Injected nuclei populations as measured using Mie scattering imaging (MSI). The natural, or pre-existing, nuclei distribution is also provided, as measured using a cavitation susceptibility meter (CSM). Both (a) cumulative and (b) non-cumulative forms are shown. In (a) the cumulative nuclei concentration, C, is plotted against the measured or equivalent bubble diameter, d, in the test section. The critical tension required to activate a nucleus, $T_c = p_c - p_v$, is also shown. In (b), the number density distribution function, $-\frac{dC}{dd}$, is plotted against bubble diameter. The monodisperse population has a dominant bubble diameter of 91 µm. The polydisperse population comprises of bubbles with a wider range of smaller diameters. Test section conditions were $\sigma = 1.6$ and $Re = 1.5 \times 10^6$.

2.4 Data processing

Optical and acoustic data corresponding to an example cavitation event are shown in Fig. 4. The composite photograph on the left shows the development of the cavity over time and is constructed from sections of multiple exposures stitched together.

2.4.1 Optical data processing

Image processing was carried out using MATLAB software. The cavity trajectory was measured from a photograph of a developed tip vortex cavity. Bounds were set to ±10 pixels (i.e. ±2.8 mm) of the trajectory and are denoted by the burgundy lines on the composite photograph in Fig. 4a. The distance along the cavity trajectory downstream of the tip, s, is normalised by c in this analysis (i.e. s/c). The maximum pixel intensity within the bounds at each spanwise location along the vortex trajectory was extracted from each video frame, and used to construct space-time datasets that show cavity development. A binary image was generated using an intensity filter to distinguish bright pixels from the background (i.e. non-cavitating conditions). Pixel intensity distributions for non-cavitating conditions were used to set the intensity threshold. Morphological image processing was used to minimise noise in the image, then an area filter was applied to identify each cavity and exclude spurious detections. The locations of the upstream and downstream extents of the cavity were extracted and analysed to obtain the cavity kinematics. The cavity length, L, is the distance between these extents, while the elongation rate, $\dot{L}$, is the first time derivative of the length.

The temporal evolution of the cavity length and elongation rate are shown in Figs. 4c and 4d, respectively. The location of TVC inception downstream of the hydrofoil tip, s_i/c, was defined as the position of the cavity at its earliest appearance and is labelled '1' in Fig. 4b. In a check of 10% of the high speed video runs, 9 cavities were detected with lengths between 0.28 (the optical resolution) and 3.0 mm. Of these, two-thirds were categorised as other entities such as out-of-focus bubbles or solid particles. The few TVC events detected in this size range account for only a very small proportion of the $\mathcal{O}(1000)$ cavities longer than 3 mm detected across these runs. Therefore, only cavities which grow to a maximum length, L_max, of over $0.02c$ (3 mm) were used for the analysis. The maximum elongation rate, $\dot{L}_\mathrm{max}$, usually occurs within 1 ms of the optical detection of inception (i.e. 16 high speed video frames).

The cavity grows axially to a maximum length of about $0.4c$ at the point indicated '3' in Fig. 4b, when the cavity head, or upstream extent, is about one chord length downstream of the tip, before contracting axially to a remnant bubble that is transported downstream, annotated '5'. Dissolved air can diffuse into the cavity in the low pressure zone, and while vapour condenses in the pressure recovery region, the air may not dissolve, resulting in a remnant bubble (Brennen, 1995).

The cavity advection velocity, U_c, is the gradient of a line connecting the start and the end of the cavity in the space-time data, as shown in Fig. 4b with a black, dashed line. It represents the mean advection velocity of the cavity head. It will be shown later that the advection velocities of the main cavity and remnant bubble can differ.

The merging and splitting of isolated cavities is common at lower cavitation numbers. Cavity splitting during the later stages of cavity development has been studied (Choi and Chahine, 2004), with the downstream segment travelling faster than the main cavity (Arndt and Maines, 2000). The cavity advection velocities presented in the results include cavities that split into multiple cavities downstream. In order to quantify the kinematic properties of isolated events, merged events are not included in the cavity kinematics results. Note that the maximum elongation rate is extracted from kinematic data prior to the merge or split, if either occurs.

2.4.2 Acoustic data processing

The pressure, P, time series measured using the hydrophone was high-pass filtered with a cut-off frequency of 1 kHz (to exclude tunnel-related noise) and is provided in Fig. 4e. The highest acoustic pressure pulse typically occurs within 5 ms of the optical detection, after the cavity has entered the cylindrical growth phase. As such, the acoustic properties of inception events were analysed using a slightly wider window of hydrophone data. The acoustic data comprised 9.8 ms (1950 samples), starting 0.8 ms prior to the optical detection of a cavity. The starting offset was corrected for the propagation delay based on the measured inception location and the sound speed. Power spectral densities (PSDs) were calculated by applying a single Hanning window to the unfiltered acoustic data for each inception event and normalising the signal power as described by Welch (1967). Non-cavitating noise was extracted from the same acquisition run using the same 9.8 ms window length and Hanning window. The PSDs of multiple sequences of non-cavitating noise data were averaged to generate representative spectra. The sound pressure levels (SPLs) of individual cavitation events were determined by integrating the PSD between 1 and 100 kHz, the Nyquist frequency. A reference pressure of 1 μPa was used to express the SPL in decibels.

The temporal separation between some cavities was so small that the acoustic pulses they generated could not be distinguished. For the monodisperse nuclei population, about 38% of cavitation events fell into this category at the lowest cavitation number of 1.6, decreasing to 5% at the highest cavitation number of 2.4. Acoustics data for such events have been omitted from the acoustic analysis.

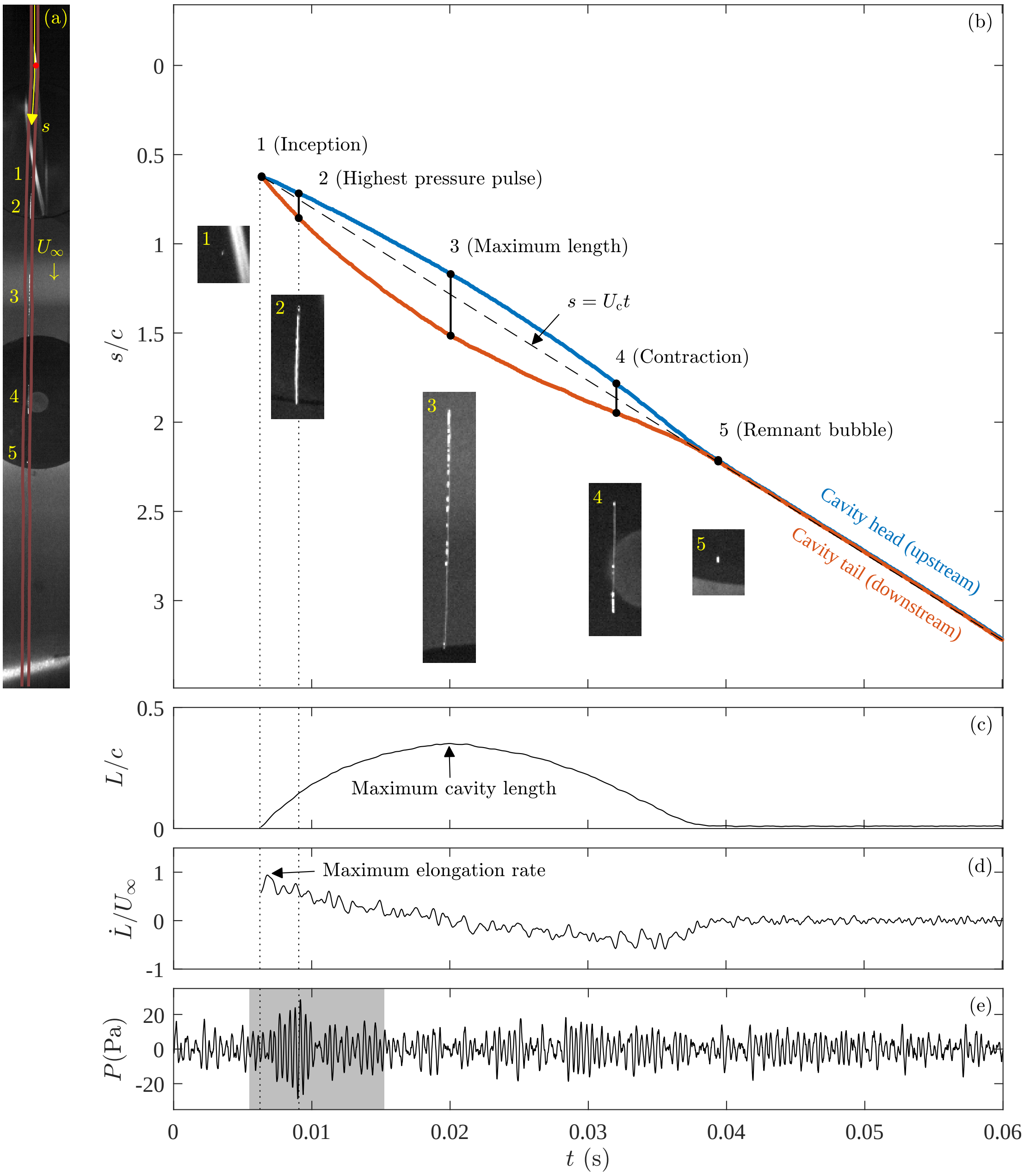

Fig. 4 Spatial and acoustic measurements of a single cavitation event ($\sigma = 1.6$, monodisperse). The (a) multiple-exposure composite photograph shows different stages of cavity development: (1) inception, (2) highest pressure pulse, (3) maximum length, (4) contraction, and (5) remnant bubble. The red dot denotes the hydrofoil tip. Data were extracted from within the bounds denoted by the burgundy lines either side of the trajectory. The distance along the cavity trajectory, s, is plotted in the (b) space-time graph, which shows cavity development over time, t. The blue and orange lines denote the positions of the cavity head and tail, respectively. Inception occurs at $s_\mathrm{i}/c = 0.62$, where s_i is the distance along the cavity trajectory, downstream of the tip, that inception occurs. The cavity advection velocity, U_c, is the gradient of the dashed line. Enlarged images of the cavity at the different stages are inset. The evolution of the (c) cavity length, L, and (d) cavity elongation rate, $\dot{L}$, are provided. The (e) time series of the acoustic pressure measurement, P, is high-pass filtered with a cut-off frequency of 1 kHz. The grey region denotes the duration of hydrophone data used for acoustics processing. The left and right vertical dotted lines are drawn at the time of inception and the highest pressure pulse, respectively.

3 Results and discussion

3.1 Optical measurements

3.1.1 Event rates and estimates of vortex properties

The number of cavitation events detected using high speed photography, and acquisition duration are provided in Table 1 for each test condition. For the nuclei population comparison at a cavitation number of 1.6, $\mathcal{O}(1000)$ events were recorded in multiple 30.6 s blocks of video data. Single 30.6 s blocks were used for each of the higher cavitation numbers for the cavitation number comparison, resulting in $\mathcal{O}(100)$ events being recorded at each of those test conditions. The cavitation event rate for each test condition is shown in Fig. 5. For the monodisperse case, the event rate increases with decreasing cavitation number. This is unsurprising as the cavitation number was lowered by reducing the test section pressure. This in turn lowered the vortex core pressure resulting in a longer streamwise length along which the pressure was below vapour pressure, as will be shown in Sect. 3.1.2. Extrapolation of these data suggests that the incipient cavitation number is at least 2.5. The minimum pressure coefficient in the vortex, $C_{\mathrm{p,min}}$, can be defined as

$$C_{\mathrm{p,min}} = \frac{p_{\mathrm{min}} - p_{\infty}}{q}, \tag{1}$$

where p_{min} is the minimum pressure in the vortex.

As the critical pressures of the monodisperse nuclei are essentially vapour pressure, then assuming the pressure in the core is vapour pressure (for the incipient case of $\sigma = 2.5$), a minimum pressure coefficient in the vortex core can be obtained by

$$\begin{aligned} C_{\mathrm{p,min}} &= \frac{p_{\mathrm{v}} - p_{\infty}}{q} \\ &= -\sigma \\ &= -2.5. \end{aligned} \tag{2}$$

For cavitation numbers less than 2.5, the highest tension, T, generated by the vortex may then be inferred as

$$\begin{aligned} T &= p_{\mathrm{min}} - p_{\mathrm{v}} \\ &= C_{\mathrm{p,min}} q + p_{\infty} - p_{\mathrm{v}}. \end{aligned} \tag{3}$$

And since

$$p_{\infty} = \sigma q + p_{\mathrm{v}}, \tag{4}$$

the tension is

$$\begin{aligned} T &= C_{\mathrm{p,min}} q + \sigma q + p_{\mathrm{v}} - p_{\mathrm{v}} \\ &= q \left(C_{\mathrm{p,min}} + \sigma \right), \end{aligned} \tag{5}$$

Table 1 Cavitation event count and acquisition duration for each test condition.

Nuclei population	σ	Event count	Duration (s)
Monodisperse	2.4	126	30.6
Monodisperse	2.2	233	30.6
Monodisperse	2.0	418	30.6
Monodisperse	1.8	614	30.6
Monodisperse	1.6	6621	275.4
Polydisperse	1.6	1662	550.8

which, for the lowest freestream cavitation number presented in this paper, $\sigma = 1.6$, corresponds to $-0.9q$, or $-50\,\mathrm{kPa}$ (absolute).

With the estimated minimum vortex pressure of $p_{\mathrm{min}} = -48\,\mathrm{kPa}$ and the lift coefficient, $C_{\mathrm{L}} = 0.44$ from force measurements, it is possible to estimate the vortex core radius for $\sigma = 1.6$. Firstly, the mid-span bound circulation, Γ_0, is defined as

$$\Gamma_0 = \frac{1}{2} C_{\mathrm{L}} U_{\infty} c. \tag{6}$$

Assuming the circulation in the tip vortex flow, Γ_{tip}, is $0.3\Gamma_0$, and a Rankine vortex model (Franc and Michel, 2006), the core radius at the location of minimum pressure, a, is estimated to be 1.2 mm using

$$a = \frac{\Gamma_{\mathrm{tip}}}{2\pi \sqrt{\frac{p_{\infty} - p_{\mathrm{min}}}{\rho}}}. \tag{7}$$

The core diameter is then about 10–100 times larger than those of the injected nuclei. Two-dimensional simulations of a Rankine vortex using the approach of Paul et al. (2021) show the diameter of the streamtube of ingested nuclei to be $\mathcal{O}(10)$ mm, which is an order of magnitude larger than the core size.

The cumulative nuclei populations presented in Fig. 3(a) suggest there are as many nuclei in the polydisperse population compared to the monodisperse. However, Fig. 5 shows that the rate of nuclei activations are some eight times greater in the monodisperse case. This indicates that radial ingestion and activation of nuclei along the vortex is biased towards the larger bubbles. This filtering of the polydisperse bubble population is due to the increase in the radial ingestion force with the cube of the bubble radius (Oweis et al., 2005), such that the larger monodisperse microbubbles are more readily drawn into the vortex.

3.1.2 Inception location

Spatial distributions of the event rate along the vortex trajectory are given in Fig. 6(a) for different nuclei populations. The event rates corresponding to the monodisperse population are higher than for the polydisperse

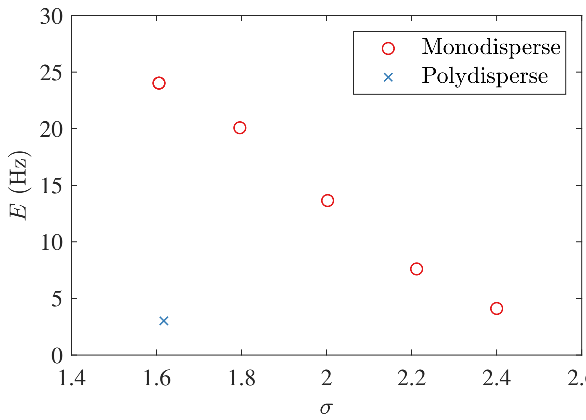

Fig. 5 Effect of cavitation number, σ, and nuclei population on inception event rate, E, for test conditions investigated in this study. The event rate decreases with increasing cavitation number for the monodisperse nuclei population. The rate corresponding to the monodisperse case is eight times higher than that of the polydisperse for the same test section conditions.

case across the range of inception locations observed. This is attributed to the higher concentration of nuclei that are captured. The distributions trend similarly. The highest event rates occur between the tip and $0.2c$ downstream, which is consistent with the location of the minimum pressure, as discussed in Sect. 1. The event rate gradually decreases till about $1c$ downstream, from which point the rate decreases steeply. For both nuclei populations, the most upstream inception location was about $0.05c$ upstream of the tip. The most downstream inception locations were $2.4c$ and $3.1c$ downstream of the tip for the monodisperse and polydisperse populations, respectively. However, the four most downstream non-zero bins of each distribution represent only 12 out of the 8283 total recorded events, so the most downstream locations quoted are only indicative. Overall, 95% of all inception events occurred less than 1.04 and $0.96c$ downstream of the tip for the mono- and polydisperse cases, respectively.

Some notable differences were observed in the results when compared to those of a similar experiment conducted by Khoo et al. (2020a). In that study, the inception location histogram corresponding to the monodisperse population was relatively uniform between the tip and $0.6c$ downstream, while a prominent peak between the tip and $0.2c$ downstream was observed for the polydisperse case. For the current dataset, there is greater similarity between the shapes of the distributions. While there is no clear explanation for this, the earlier study differed with respect to a number of aspects. Although sample sizes were similar, the data acquisition method (image-based trigger instead of block recording) and monodisperse nuclei size (75 µm dominant bubble diameter instead of 91 µm) used, were not. It should also be noted that the image-based trigger used for the earlier investigation was positioned at $2.4c$, which precluded the detection of inception events further downstream.

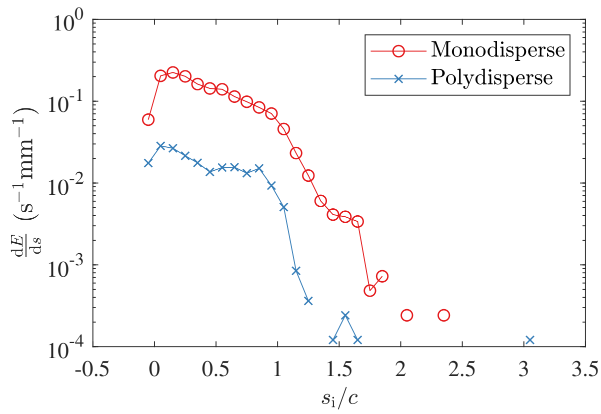

(a) Nuclei population effect, $\sigma = 1.6$

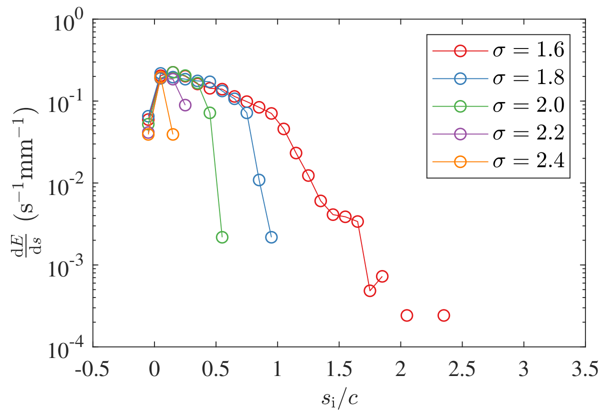

(b) Cavitation number, σ, effect (Monodisperse)

Fig. 6 Effect of inception location, s_i/c, on inception event rate density, $\frac{dE}{ds}$, for different (a) nuclei populations and (b) cavitation numbers. A bin width of $0.1c$ is used to construct the histograms and markers are located at the middle of each non-zero bin. Higher event rates are observed for the monodisperse nuclei population compared to the polydisperse. In both cases, the event rate peaks just downstream of the hydrofoil tip and decreases with increasing inception distance from the tip. The range of locations downstream of the tip at which inception occurs increases with decreasing cavitation number. Inception happens most often just downstream of the tip for all cavitation numbers tested.

The effect of cavitation number on inception location is illustrated in Fig. 6(b). The monodisperse population was used for this investigation and the cavitation number was changed via the test section pressure. Inception occurs further downstream with decreasing cavitation number, with an increasing length of vortex along which the local pressure is sufficiently low to activate captured nuclei. Meanwhile, the event rate near

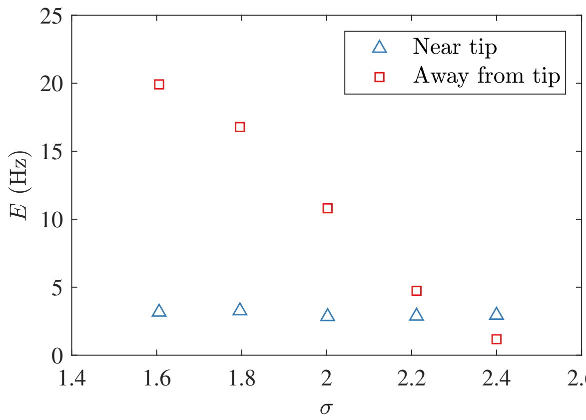

Fig. 7 Effect of cavitation number, σ, on inception event rate, E, at different inception locations in a flow with an injected monodisperse nuclei population. The event rate between the tip and 0.1 chord lengths downstream is independent of cavitation number. Away from the tip, the rate decreases with increasing cavitation number.

the tip remains relatively unchanged with cavitation number. These trends are shown with greater clarity in Fig. 7. This indicates that even at the highest cavitation number tested, the local pressure near the tip is sufficiently low to activate all monodisperse nuclei captured here. A reduction in the cavitation number does not lead to the cavitation of any additional nuclei at this location as all monodisperse nuclei were also activated at the highest cavitation number. It does, however, result in a longer portion of the trailing vortex being under tension, and thus additional activations occur downstream.

3.1.3 Effect of inception location on maximum cavity length

The influence of inception location on maximum cavity length is shown for the two nuclei populations (see Fig. 8(a)). From Fig. 8, a bin width of $3.8 \times 10^{-3}c$, or 0.57 mm, is used for inception location data. Merged cavities form when two or more isolated cavities join, resulting in a longer cavity. Many were observed at the lowest cavitation number. However, only isolated cavities are included in Fig. 8. The highest maximum lengths ranging between 1 and $2c$ occur between $-0.05c$ and $0.28c$. The inclusion of merged cavities increases the peak by only 5%, which shows that the longest incipient cavity that can be sustained in the tip vortex is about $2c$ in length. The scatter in the maximum length data is highest near the location of the peak. The maximum length then decreases with increasing downstream distance. In general, the nuclei population does not affect the behaviour of the maximum cavity length. The mono- and polydisperse datasets exhibit similar degrees of scatter, noting that the sample size is about four times larger for the former.

In contrast, cavitation number has a significant effect on maximum cavity length (see Fig. 8(b)). The maximum length increases with decreasing cavitation number. For the cavitation numbers above 1.6, the peak maximum lengths occur across a smaller range of inception locations (i.e. between $-0.04c$ and the tip). The maximum length decreases with increasing inception distance downstream and at a higher rate at lower cavitation numbers. It is evident that the local pressure, rather than the initial bubble size, determines the maximum length of the cavity.

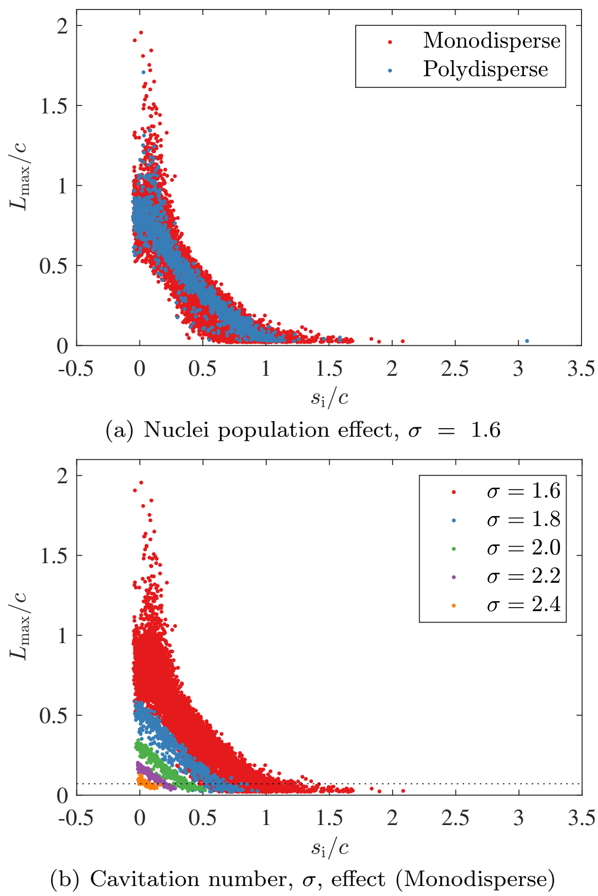

Fig. 8 Effect of inception location, s_i/c, on maximum cavity length, $L_{\max}/c$, for different (a) nuclei populations and (b) cavitation numbers. The maximum cavity length decreases with increasing inception distance downstream from the tip and increasing cavitation number. The trend is independent of nuclei population. The dotted line in (b) corresponds to the mean $L_{\max}/c$ for $\sigma = 2.4$ and is used to infer the streamwise pressure distribution in Fig. 10.

3.1.4 Effect of streamwise location on maximum cavity elongation rate

The effect of streamwise location on maximum cavity elongation rate is illustrated in Fig. 9(a) for different nuclei populations. The highest maximum elongation rates ranging from 2.4 to $2.6U_\infty$ occur between -0.01 and $0.1c$ downstream of the tip. It decreases linearly to about $1.2c$ and subsequently asymptotes to about $0.16U_\infty$. The rate tends to decrease upstream of $0.02c$.

There are a group of inception events with lower elongation rates labelled 'Data 1' in Fig. 9(a) that sit below the main band of data. Inspection of these outlying events reveals that they incept upstream of existing cavities and grow to a maximum length of about $0.4c$. This appears to be a consequence of cavity interaction effects and illustrates how existing cavities can suppress the elongation rate of new ones. The initial nucleus size has no significant effect on the maximum elongation rate.

The effect of cavitation number on maximum cavity elongation rate is shown in Fig. 9(b). Again, the cavitation number is shown to have a greater effect on cavity dynamics than the initial nucleus size. The maximum elongation rate increases with decreasing cavitation number. For all cavitation numbers, the maximum elongation rate tends to decrease with increasing distance downstream, reflecting the effect of the change of local pressure in the vortex on cavity dynamics. The slope of the reduction of the maximum elongation rate with increasing inception distance downstream of the tip increases with increasing cavitation number. This is in contrast with the maximum length data. For all cavitation numbers tested, the highest maximum elongation rate occurs between the tip and $0.04c$ downstream. The downstream asymptotic behaviour observed for the cavitation numbers of 1.6 and 1.8 cannot be observed for higher cavitation numbers of 2.0 and above.

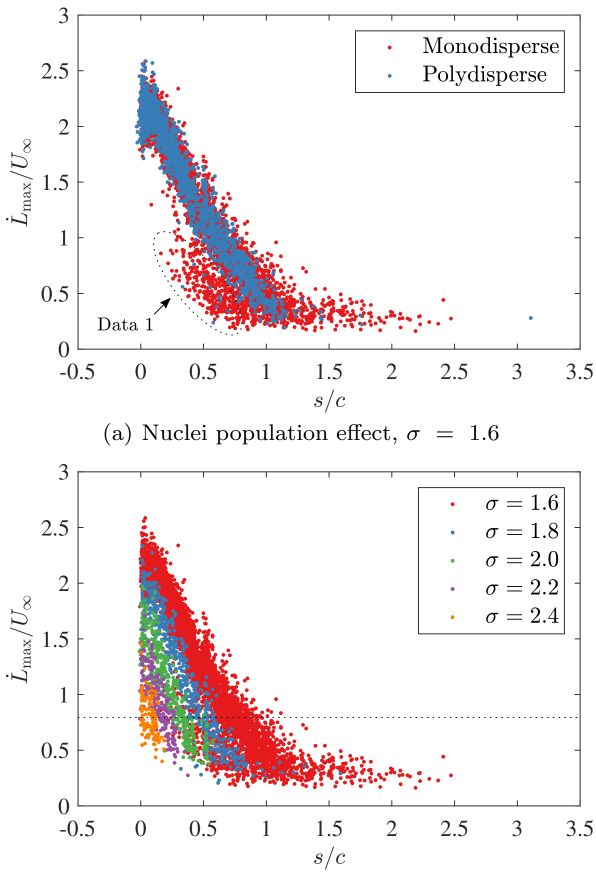

(a) Nuclei population effect, $\sigma = 1.6$

(b) Cavitation number, σ, effect (Monodisperse)

Fig. 9 Effect of streamwise location, s/c, on maximum cavity elongation rate, $\dot{L}_{\max}/U_\infty$, for different (a) nuclei populations and (b) cavitation numbers. The highest maximum elongation rates occur near the tip. The rate decreases with increasing distance from the tip and increasing cavitation number. Nuclei population has no significant effect on the maximum elongation rate. The dotted line in (b) corresponds to the mean $\dot{L}_{\max}/U_\infty$ for $\sigma = 2.4$ and is used to infer the streamwise pressure distribution in Fig. 10. Data labelled 'Data 1' represent shorter cavities that incept upstream of existing cavities.

3.1.5 Streamwise pressure distribution

The streamwise pressure distribution was inferred from the maximum cavity length and elongation rate data (see Fig. 10). The average inception or streamwise location corresponding to the mean maximum length and elongation rate was determined for the $\sigma = 2.4$ data in Figs. 8(b) and 9(b). It is assumed that the local pressure here is vapour pressure, and is sufficient to activate the monodisperse nuclei population. Then the streamwise location corresponding to the same maximum length and elongation rate was identified for each of the lower cavitation numbers. The local pressures at these locations are also assumed to be vapour pressure. Therefore, the local pressure coefficient at each streamwise location is simply the negative of the corresponding cavitation number.

It was inferred from the event rate data in Fig. 5 that the minimum pressure coefficient is -2.5, and the streamwise pressure distribution in Fig. 10 shows that the minimum pressure coefficient occurs near the tip and recovers to -1.6 at about 0.8 chord lengths downstream. The rate of pressure recovery decreases with increasing distance downstream. The pressure distribution changes slightly depending on the kinematic property used, although the overall trends are similar and comparable to those observed in simulations (Chen et al., 2019; Asnaghi et al., 2020) and inferred from experimental measurements (Fruman and Dugue, 1994) of elliptical hydrofoils. Additional direct measurements of the vortex core pressure using an identical foil geometry and operating conditions would be useful to validate the inferred pressure distributions in Fig. 10.

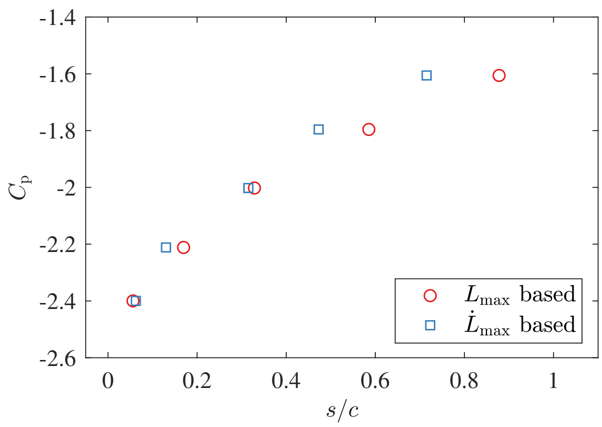

Fig. 10 Pressure coefficient, C_p, as a function of location along the vortex, s/c, inferred from maximum cavity length, L_{max}, and maximum elongation rate, $\dot{L}_{max}$, data in Figs. 8(b) and 9(b), respectively. The pressure is lowest near the tip, and the rate of recovery decreases with distance downstream.

3.1.6 Effect of inception location on cavity advection velocity

The influence of inception location on cavity advection velocity is shown in Fig. 11. As described in Sect. 2.4.1, this parameter represents the mean advection velocity of the cavity head along the vortex trajectory. Nuclei population has no significant effect on cavity advection velocity. Tip vortex cavities tend to have higher advection velocities when inception occurs further downstream. The outliers with advection velocities between 0.8 and $1U_\infty$ and inception locations between 0.5 and $1c$ downstream of the tip, denoted ‘Data 2’, are mainly associated with relatively short cavities that incept downstream of existing longer cavities. This suggests that existing cavities alter the flow field such that new ones that incept downstream travel at higher advection velocities compared to isolated cavities. Inception events near the tip with advection velocities lower than $0.6U_\infty$, denoted ‘Data 3’, correspond to long, isolated cavities for which the cavity head initially migrates downstream at a much slower rate than the cavity tail.

The effect of cavitation number on the cavity advection velocity behaviour is shown in Fig. 11(b). Again, the cavitation number is found to influence the cavity dynamic properties more than the initial nucleus size. Higher advection velocities occur with increasing cavitation number and increasing inception distance downstream of the tip. For the highest cavitation number, the cavity advection velocity can exceed that of the freestream. It is deduced from Figs. 8(b) and 11(b) that the size or inertia of a smaller cavity allows it to travel at a higher velocity. Cavity length is determined by the local pressure which is controlled by the cavitation number and the streamwise position at inception, as demonstrated in Sect. 3.1.3.

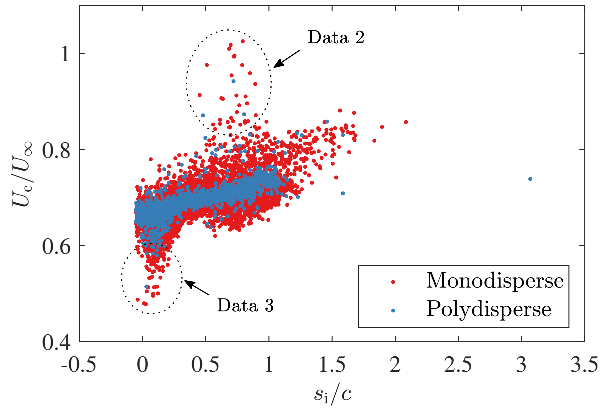

(a) Nuclei population effect, $\sigma = 1.6$

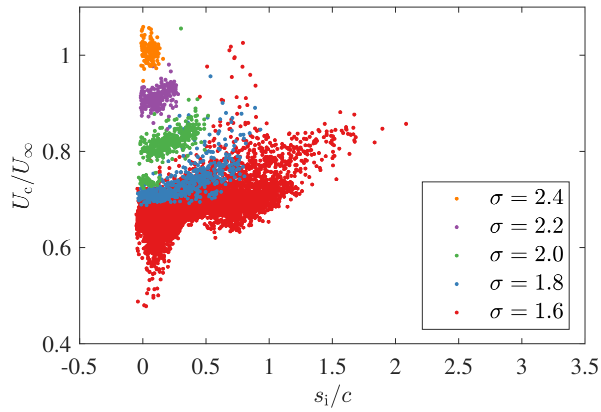

(b) Cavitation number, σ, effect (Monodisperse)

Fig. 11 Effect of inception location, s_i/c, on cavity advection velocity, U_c/U_∞, for different (a) nuclei populations and (b) cavitation numbers. The advection velocity tends to increase with increasing inception distance from the tip and increasing cavitation number. The trend is generally independent of nuclei population. Data labelled ‘Data 2’ represent shorter cavities that incept downstream of existing longer cavities, and ‘Data 3’ denotes long cavities.

Given that tip vortex cavity development is comprised of multiple stages, as demonstrated in Fig. 4, cavity advection velocity was investigated in additional detail. Rather than calculating the cavity advection velocity based on the entire cavity region identified in the space-time plot, two velocities were calculated for an event: one for the main body of the cavity comprising both growth and contraction phases, U_{c1}, and one for the remnant bubble, U_{c2}. The spatial histories of some example cavities are given in Fig. 12, showing typical cavities that incepted near the tip for each of the cavitation numbers, as well as two downstream inception events for a cavitation number of 1.6. Cavity regions for a number of example events are plotted, annotated with corresponding advection velocities. If the remnant bubble was not detected by the image processing method, its location was determined by inspection, and is shown by a dashed line drawn between it and the cavity.

The advection velocity of the main body trends in the same way with cavitation number and inception location as illustrated in Fig. 11(b). Higher main body advection velocities are found for cavities with shorter maximum lengths. These maximum lengths vary with cavitation number and inception location in the same manner as presented in Fig. 8(b). The advection velocity of the remnant bubble is about $0.7U_\infty$ and is independent of cavitation number and inception location, suggesting it is not cavitation-related. It may, however, indicate a constant axial velocity deficit in the vortex core, although the effect of the cavity on the axial velocity distribution in the vortex core has not been quantified.

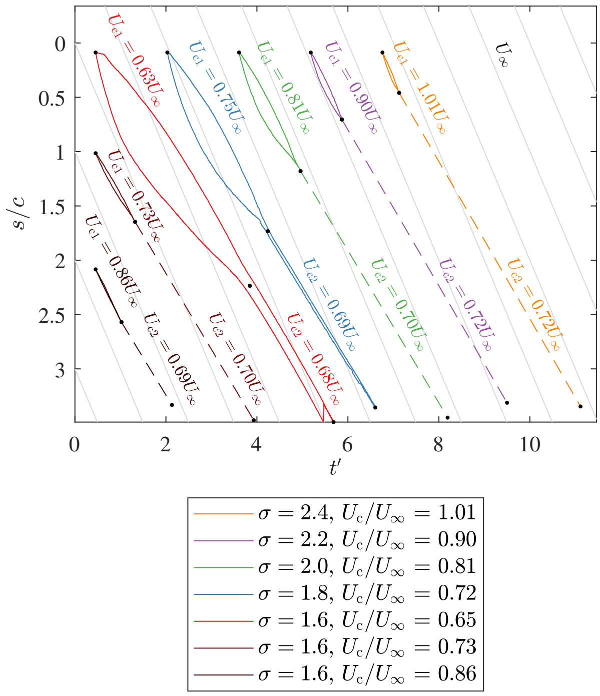

Fig. 12 Space-time plot of example cavities showing the effects of cavitation number and inception location on the main cavity body advection velocity, U_{c1}, and remnant bubble advection velocity, U_{c2}. Cavity advection velocities, U_c, defined using the entire cavity region are also provided for each cavity. All velocities are expressed as a proportion of the freestream velocity, U_∞. Nondimensional time, $t' = t/U_\infty c$, is shown on the x-axis. The freestream velocity is represented by the solid, grey lines. The black dots are the coordinates used to derive the advection velocities, as explained in the text. The main body advection velocity increases with increasing cavitation number and increasing inception distance downstream of the tip, and thus decreasing maximum length. The remnant bubble advection velocity is about $0.7U_\infty$, independent of cavitation number and inception location.

3.2 Acoustic measurements

3.2.1 Sound pressure levels

The effect of inception location on the sound pressure level (SPL) of inception events is shown in Fig. 13(a) for different nuclei populations. The hydrophone was located $0.2c$ downstream of the tip and is marked with a vertical, dashed line in the figure. The nuclei population has no significant effect on the SPL behaviour. The highest pressure pulses occur when inception is near the tip and decrease in amplitude with increasing inception distance downstream. The maximum SPLs ranging from 152 to 153 dB occur when inception occurs between 0.05 and $0.14c$ downstream, which is similar to where the highest cavity elongation rates were observed in Sect. 3.1.4, albeit delayed by about $0.05c$. Given this similarity, the SPL and maximum elongation rate were plotted against each other to examine their relationship (see Fig. 13(b)). For maximum elongation rates up to about $1.7U_\infty$, the SPL increases with increasing maximum elongation rate. This is consistent with the theory that higher growth rates contribute to higher pressure pulse amplitudes (Lamb, 1945). Beyond $1.7U_\infty$, there is a higher degree of scatter. In this range, 90% of the events with lower SPL comprised of cavities that incept upstream of the tip, with the remainder incepting up to $0.25c$ downstream of the tip. Meanwhile, higher SPLs were measured for other cavities with similar maximum elongation rates that incept downstream of the tip. The lower SPLs might be explained in part by the relative positions of the hydrophone, hydrofoil and cavity. The hydrofoil may attenuate the acoustic pressure pulse generated for events that incept near the tip.

The effect of cavitation number on SPL is shown in Fig. 14(a). Inception events become quieter with increasing cavitation number and increasing distance downstream of the tip. The higher maximum elongation rates observed at lower cavitation numbers produce higher SPLs, as seen in Fig. 14(b). Only data for cavities with inception locations between the tip and $0.15c$ downstream are shown in this figure as it is a region of interest given the higher event rates, cavity elongation rates and SPLs associated with cavities that incept here. This indicates that SPL is controlled by the elongation rate, which is a function of the local pressure.

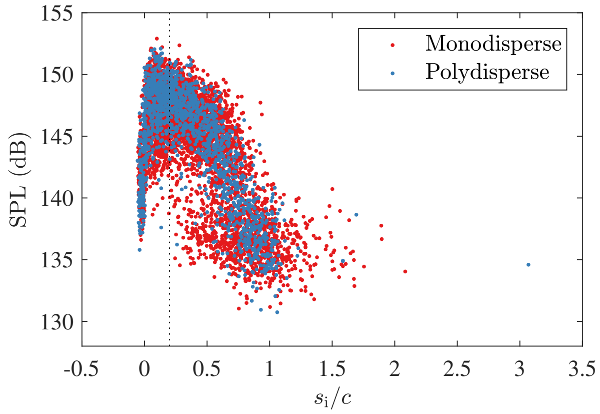

(a) Effect of inception location, s_i/c

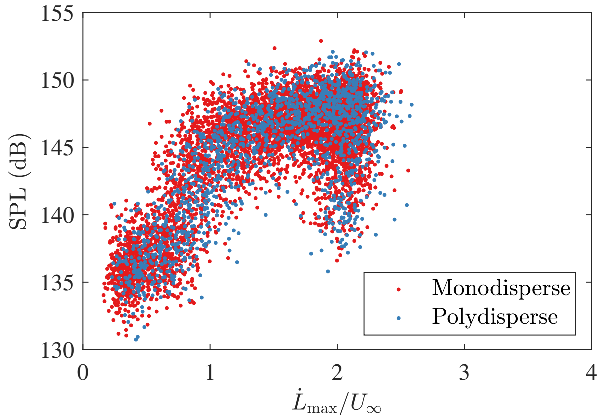

(b) Effect of maximum elongation rate, $\dot{L}_\mathrm{max}/U_\infty$

Fig. 13 Effect of (a) inception location and (b) maximum cavity elongation rate on the sound pressure level (SPL) of inception events ($\sigma = 1.6$). The SPL is calculated using the integral of the power spectral density between 1 and 100 kHz and includes background noise. The hydrophone location is 0.2 chord lengths downstream of the tip, and is denoted by the dotted line in (a). The maximum SPL occurs between 0.05 and 0.14c downstream of the tip, with a sharp reduction further upstream and gradual decrease with increasing inception distance downstream. Nuclei population has no significant effect on SPL.

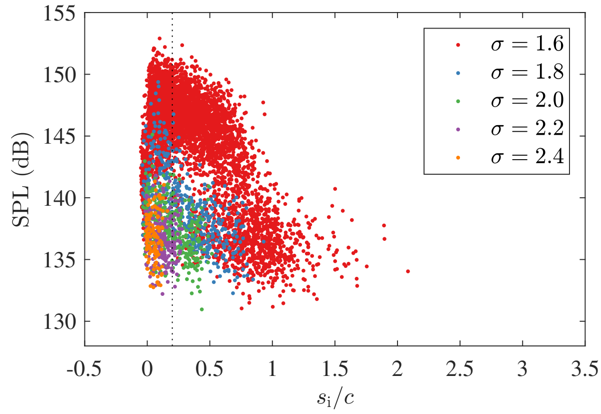

(a) Effect of inception location, s_i/c

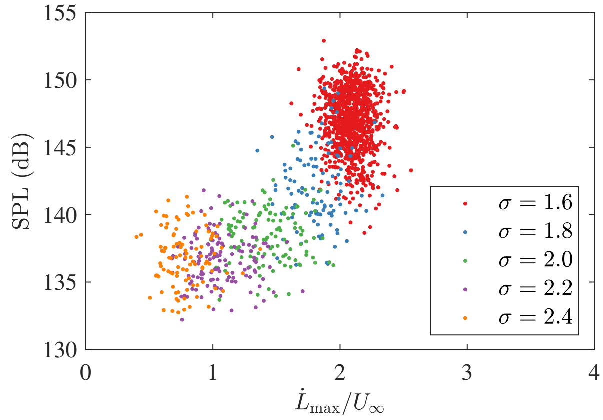

(b) Effect of maximum elongation rate, $\dot{L}_\mathrm{max}/U_\infty$

Fig. 14 Effect of (a) inception location and (b) maximum cavity elongation rate on the sound pressure level (SPL) of inception events (monodisperse). The SPL is calculated using the integral of the power spectral density between 1 and 100 kHz and includes background noise. The hydrophone location is 0.2 chord lengths downstream of the tip, and is denoted by the dotted line in (a). Only inception events that occur between the tip and 0.15 chord lengths downstream are shown in (b). The SPL is higher at lower cavitation numbers and for higher maximum elongation rates.

3.2.2 Acoustic frequency spectra

Power spectral densities of non-cavitating noise in flows with different nuclei populations are shown in Fig. 15. The polydisperse nuclei generators produce high frequency, broadband noise between 10 and 100 kHz, as well as some noise in the 5 to 6.5 kHz range.

The influence of inception location on TVC noise frequency spectra for the two nuclei populations is presented in Fig. 16. The difference between power spectral densities (PSDs) of cavitating and non-cavitating noise, ΔPSD, is shown to depict only the contribution from cavitation. As mentioned earlier, a bin width of $3.8 \times 10^{-3}c$, or 0.57 mm, is used, and data for cavities that incept in the same bin are averaged. Two strong narrow-band peaks centred at 2.27 and 2.76 kHz can be observed when inception occurs near the tip, regardless of nuclei population. The lower-frequency peak is associated with cavitation inception, and weakens by 0.6c. The peak also narrows downstream of 0.2c and its centre increases slightly to 2.36 kHz.

The peak centred at 2.76 kHz also narrows downstream of 0.6c, with its frequency shifting slightly higher to 2.82 kHz. The signal power remains relatively constant from the tip until 0.8c, at which point it decreases and disappears by 1c. Based on the results presented

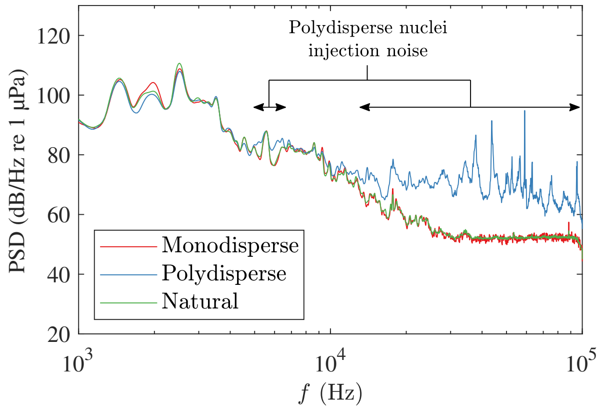

Fig. 15 Non-cavitating noise for different nuclei populations (σ = 1.6). Broadband noise above 10 kHz, and between 5 and 6.5 kHz is present for the polydisperse case due to the operation of the polydisperse nuclei generators. Neither flows with monodisperse nor natural nuclei populations exhibit such noise.

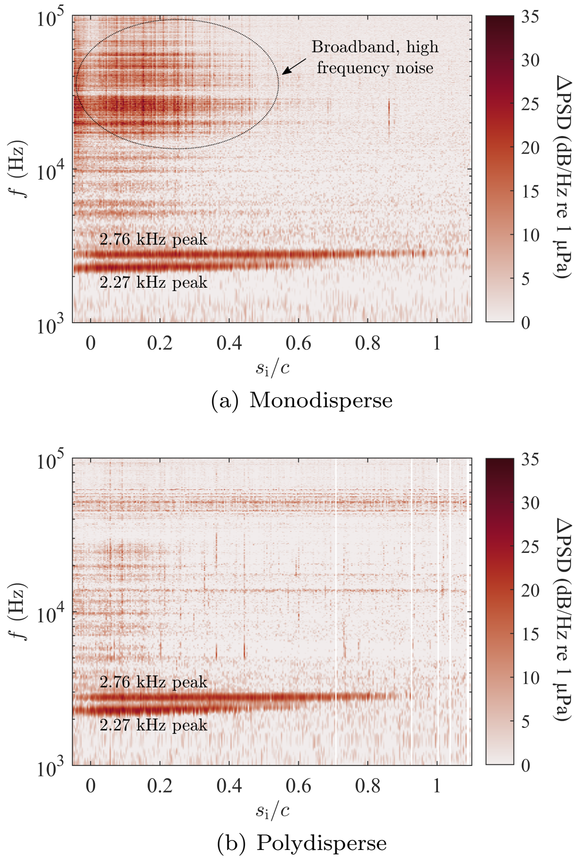

Fig. 16 Effect of inception location, s_i/c, on power spectral densities (PSDs) of inception events ($\sigma = 1.6$), in flows with (a) monodisperse and (b) polydisperse nuclei populations. The difference of cavitating and non-cavitating PSDs, ΔPSD, is presented in order to isolate cavitation noise. Data for events incepting at the same streamwise location are averaged. Two narrow-band peaks are present between the tip and 0.6 chord lengths downstream, independent of nuclei population. The higher-frequency peak persists until $s_i/c = 1$. This peak may be a tunnel-related resonant frequency. Broadband noise above 10 kHz exists for the monodisperse case, decreasing with increasing inception distance downstream from the tip.

later in Fig. 17, it is suggested that this is a tunnel-related resonant frequency excited by TVC inception events.

High frequency, broadband noise between 10 and 100 kHz can be observed for cavitation events that incept near the tip for the monodisperse case (see Fig. 16(a)). This noise subsides with increasing inception distance downstream and disappears at about 0.5c. Such noise is difficult to distinguish for the polydisperse case in Fig. 16(b), being masked by the noise of the nuclei generators as seen in Fig. 15.

The effect of cavitation number on the PSDs of inception events for the monodisperse case is presented in Fig. 17. The mean ΔPSD of inception events occurring between the tip and 0.15c downstream is shown for each cavitation number. Similarly to Fig. 14(b), only upstream inception locations are considered for this comparison as this is a region of interest given the higher event rates, cavity elongation rates and SPLs discussed earlier.

TVC acoustic characteristics are dependent on cavitation number. As discussed above, the peak at 2.76 kHz observed for a cavitation number of 1.6 may be tunnel-related. A peak at 2.81 kHz appears for a cavitation number of 1.8. This is difficult to distinguish from the potential tunnel-related peak. The peak frequency increases to 3.71, 5.05 and 6.00 kHz for cavitation numbers of 2.0, 2.2 and 2.4, respectively. The peak frequency trends with the square of the external pressure. Spherical and non-spherical bubble theory states the resonant frequency goes with the square root of the pressure (Brennen, 1995; Neppiras, 1980), however the squared relationship may be expected once bubble length, which is inversely proportional to external pressure, is taken into account. Additionally, high spatial and temporal resolution imaging of cavity surface deformations may extend existing knowledge on the relationship between cavity dynamics and acoustics. Such imaging could be used to assess the performance of cavity dynamic (Pennings et al., 2015) and acoustic (Ffowcs Williams and Hawkings, 1969; Testa et al., 2018) models. Finally, the broadband noise between 10 and 100 kHz observed for a cavitation number of 1.6 decreases with increasing cavitation number. This behaviour is similar to that of the spectral peaks at frequencies lower than 10 kHz, as discussed above.

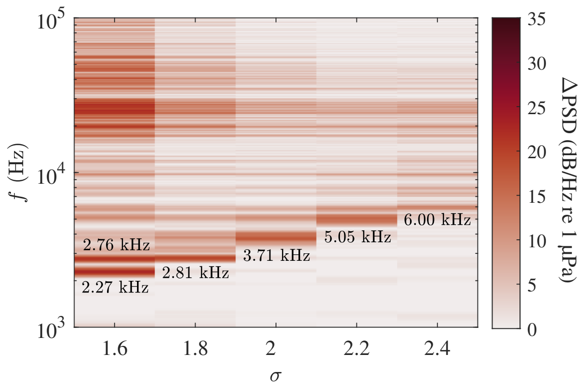

Fig. 17 Effect of cavitation number, σ, on the mean power spectral densities (PSDs) of inception events that occur between the tip and 0.15 chord lengths downstream, in a flow with monodisperse nuclei. The difference of cavitating and non-cavitating PSDs, ΔPSD, is shown in order to isolate cavitation noise. The peak frequencies of narrow-band noise are annotated either above or below the corresponding spectral bands. The peak at 2.76 kHz may be tunnel-related. The peak frequency associated with cavitation noise increases with increasing cavitation number. The broadband noise between 10 and 100 kHz reduces with increasing cavitation number.

3.2.3 Summary of results

The results presented show that the tip region plays a dominant role with respect to TVC event rate, kinematics and acoustics. This is where the longest and loudest cavities incept, and also where the highest elongation rates occur. It is inferred that the minimum pressure is located here, causing more explosive cavity growth and higher noise emission compared to when inception occurs further downstream. Changes in local pressure due to cavitation number and with inception location influence tip vortex cavity kinematics and acoustics more than nuclei population and initial nucleus size, at least across the size ranges investigated in this study. While a clear difference between inception event rates for each population was observed, it is possible that the microbubbles activated in each population are so similar in size and critical pressure that the dynamic and acoustic characteristics of individual inception events are effectively invariant. Further insight into the effects of nucleation on TVC could be gained by studying two monodisperse nuclei populations, with different dominant bubble sizes and thus critical pressures. Finally, it was assumed in this analysis that for the monodisperse case, TVC inception occurred at vapour pressure. In theory, this would be sufficient to activate the monodisperse microbubbles and produce vaporous cavitation. This could be confirmed via direct pressure measurements.

4 Conclusions

High speed video and synchronous hydrophone measurements allow the study of the spatial and acoustic characteristics of tip vortex cavitation inception. Quantitative insights were made into inception location, cavity dynamics and acoustic behaviour. Nuclei populations can substantially affect TVC inception behaviour, and were investigated using mono- and polydisperse nuclei populations, in addition to different cavitation numbers.

Nuclei population affects inception event rates due to differences in nuclei size distributions and therefore capture physics and activation rates. The shapes and ranges of the inception location distributions were observed to be similar for each nuclei population, with the highest event rate occurring near the tip. At lower cavitation numbers, the lower test section pressure results in lower vortex core pressure and a longer length of the vortex under tension, such that nuclei ingested downstream are also activated. This increases the length of the activation zone and the event rate. In a flow with relatively weak monodisperse nuclei, the event rate near the tip remains constant since all available nuclei captured in this region are also activated at higher cavitation numbers. The minimum pressure coefficient of about -2.5 occurs near the tip according to the streamwise vortex pressure distribution inferred from the cavity kinematic data. Based on the kinematic and acoustic measurements, it is concluded that the lower pressure in this region causes more explosive cavity growth and higher noise emissions.

Following activation, cavity kinematic properties are determined more by the local pressure than initial nucleus size, at least for the ∼50–100 μm diameter range considered in this study. Cavities that incept at higher tensions, whether at lower cavitation numbers or closer to the tip, grow into longer cavities. Such cavities have lower advection velocities, usually lower than the freestream velocity. Remnant bubbles are transported at about 70% of the freestream velocity independent of inception location and cavitation number.

Cavity acoustic properties are affected more by the local pressure than initial nucleus size. The sound pressure levels of inception events are highest when inception occurs near the tip and are higher at lower cavitation numbers. Further work is required to accurately measure volumetric changes during cavity growth to explain observed acoustic magnitudes.

Similar tonal peaks were measured in flows with mono- and polydisperse nuclei populations indicating the spectral content is independent of initial nucleus size. The frequency of the tonal peak increases with cavitation number. At a fixed cavitation number, the frequency remains relatively constant when inception occurs in the vicinity of the tip, but the peak decreases in power and disappears further downstream. Broadband spectral content at higher frequencies was measured for the monodisperse case when inception occurred near the tip. High spatial and temporal resolution imaging of cavity surface deformations could allow the performance of theoretical cavity dynamic and acoustic models to be assessed. It may also reveal the role of different deformation modes in tip vortex cavity noise generation.

Although the cavity kinematics and acoustics discussed above appear to be relatively independent of nuclei size, the results should be qualified by the fact that the critical pressures of bubbles in the diameter range 50–100 µm only differ by several hundred pascals. Furthermore, the two injected populations are not too dissimilar in a global sense when compared with the natural nuclei population, as shown in Fig. 3(a), which can withstand tensions beyond -100 kPa. Therefore, the similarities in the kinematic and acoustic characteristics of TVC for each nuclei population are perhaps not surprising. Further work is required to generate nuclei populations with higher tensile strengths between those of the 50–100 µm and the natural populations to better understand the influence of nuclei populations on TVC.

Authors' contributions

Conceived experiment design: M.T. Khoo, J.A. Venning, P.A. Brandner
Performed experiments: J.A. Venning, M.T. Khoo
Analysed data: M.T. Khoo, J.A. Venning
Prepared manuscript: M.T. Khoo, J.A. Venning, P.A. Brandner, B.W. Pearce

Acknowledgements The authors acknowledge the support of the University of Tasmania and the Defence Science and Technology Group. The authors thank Dr Rhys Paul for assistance with data acquisition, and AMC technical officers, Mr Robert Wrigley and Mr Steven Kent for providing technical assistance with test facility configuration and operation.

References

Arndt R, Maines B (2000) Nucleation and bubble dynamics in vortical flows. J Fluids Eng - Transactions of the ASME 122(3):488–493, DOI 10.1115/1.1286994

Arndt RE, Keller AP (1992) Water quality effects on cavitation inception in a trailing vortex. J Fluids Eng - Transactions of the ASME 114(3):430–438

Asnaghi A, Svennberg U, Bensow RE (2020) Large eddy simulations of cavitating tip vortex flows. Ocean Eng 195:106703

Astolfi JA, Fruman D, Billard JY (1999) A model for tip vortex roll-up in the near field region of three-dimensional foils and the prediction of cavitation onset. European Journal of Mechanics-B/Fluids 18(4):757–775

Brandner P, Lecoffre Y, Walker G (2007) Design considerations in the development of a modern cavitation tunnel. In: 16th Australasian Fluid Mechanics Conf

Brennen CE (1995) Cavitation and Bubble Dynamics. Cambridge University Press

Briançon-Marjollet L, Merle L (1996) Inception, development and noise of a tip vortex cavitation. In: Proc 21st Symp on Naval Hydrodynamics, pp 851–864

Chang N, Ganesh H, Yakushiji R, Ceccio SL (2011) Tip vortex cavitation suppression by active mass injection. J Fluids Eng 133(11):111301

Chen L, Zhang L, Peng X, Shao X (2019) Influence of water quality on the tip vortex cavitation inception. Phys Fluids 31(2):023303

Choi J, Ceccio SL (2007) Dynamics and noise emission of vortex cavitation bubbles. J Fluid Mech 575:1–26

Choi J, Hsiao CT, Chahine G, Ceccio S (2009) Growth, oscillation and collapse of vortex cavitation bubbles. J Fluid Mech 624:255–279

Choi JK, Chahine GL (2003) A numerical study on the bubble noise and the tip vortex cavitation inception. J Ship and Ocean Tech 7(3):13–33

Choi JK, Chahine GL (2004) Noise due to extreme bubble deformation near inception of tip vortex cavitation. Phys Fluids 16(7):2411–2418

Doolan C, Brandner P, Butler D, Pearce B, Moreau D, Brooks L (2013) Hydroacoustic characterisation of the AMC cavitation tunnel. In: Acoustics 2013 Victor Harbor - Science, Technology and Amenity, Victor Harbor, Australia, The Australian Acoustical Society, pp 1–7

Ffowcs Williams J, Hawkings DL (1969) Sound generation by turbulence and surfaces in arbitrary motion. Philosophical Transactions for the Royal Society of London Series A, Mathematical and Physical Sciences pp 321–342

Fitzpatrick HM (1958) Cavitation noise. In: 2nd Symp on Naval Hydrodynamics, Washington

Franc JP, Michel JM (2006) Fundamentals of Cavitation. Springer Science & Business Media

Fruman D, Dugue C (1994) Tip vortex roll-up and cavitation. In: Proc 19th Symp on Naval Hydrodynamics, pp 633–654

Gindroz B, Billet M (1998) Influence of the nuclei on the cavitation inception for different types of cavitation on ship propellers. J Fluids Eng 120(1):171–178

Gindroz B, Billard JY, Geistdoerfer P (1995) Cavitation nuclei measurements at sea. ASME Publications HTD 321:497–504

Giosio D, Pearce B, Brandner P (2016) Influence of pressure on microbubble production rate in a confined turbulent jet. In: 20th Australasian Fluid Mechanics Conf

Gowing S, Shen YT (2001) Nuclei effects on tip vortex cavitation scaling. In: 4th Int Symp on Cavitation, California

Higuchi H, Arndt R, Rogers M (1989) Characteristics of tip vortex cavitation noise. J Fluids Eng 111:495–501

Hsiao CT, Chahine GL (2005) Scaling of tip vortex cavitation inception noise with a bubble dynamics model accounting for nuclei size distribution. J Fluids Eng 127(1):55–65

Johnson BD (1986) Bubble populations: background and breaking waves. In: Oceanic Whitecaps, Springer, pp 69–73

Khoo M, Venning J, Pearce B, Brandner P (2018) Nucleation effects on hydrofoil tip vortex cavitation. In: 21st Australasian Fluid Mechanics Conf

Khoo M, Venning J, Pearce B, Brandner P (2020a) Nucleation effects on tip vortex cavitation inception location. In: 22nd Australasian Fluid Mechanics Conf, The University of Queensland

Khoo M, Venning J, Pearce B, Brandner P (2020b) Statistical aspects of tip vortex cavitation inception and desinence in a nuclei deplete flow. Exp Fluids 61(6)(145):1–13

Khoo M, Venning J, Pearce B, Takahashi K, Mori T, Brandner P (2020c) Natural nuclei population dynamics in cavitation tunnels. Exp Fluids 61(2)(34):1–20

Lamb H (1945) Hydrodynamics. Dover Publications

Leighton T (2012) The acoustic bubble. Academic press

Ligneul P, Latorre R (1989) Study on the capture and noise of spherical nuclei in the presence of the tip vortex of hydrofoils and propellers. Acta Acustica united with Acustica 68(1):1–14

Ligneul P, Latorre R (1993) Study of nuclei distribution and vortex diffusion influence on nuclei capture by a tip vortex and nuclei capture noise. J Fluids Eng 115(3):504–507

Maines B, Arndt R (1993) Bubble dynamics of cavitation inception in a wing tip vortex. In: ASME Cavitation and Multiphase Flow Forum, FED, 1993, vol 153, pp 93–97

Minnaert M (1933) XVI. On musical air-bubbles and the sounds of running water. The London, Edinburgh, and Dublin Philosophical Magazine and Journal of Science 16(104):235–248

Neppiras EA (1980) Acoustic cavitation. Physics reports 61(3):159–251

O'Hern T, Green S, Morss E (1986) Measurements of oceanic nuclei distributions. In: ASME Cavitation and Multiphase Flow Forum, pp 23–26

Oweis G, van der Hout I, Iyer C, Tryggvason G, Ceccio S (2005) Capture and inception of bubbles near line vortices. Phys Fluids 17(2)

Paul R, Venning J, Pearce B, Brandner P (2021) Nuclei transport about a sphere. In: 11th Int Symp on Cavitation (CAV2021), Daejon, Korea

Peng X, Xu L, Cao Y (2017) The study of tip vortex flow and cavitation inception on an elliptical hydrofoil. In: Proc of Fifth Int Symp on Marine Propulsion, Espoo, Finland

Pennings P, Bosschers J, Westerweel J, Van Terwisga T (2015) Dynamics of isolated vortex cavitation. J Fluid Mech 778:288–313

Russell P, Giosio D, Venning J, Pearce B, Brandner P, Aumelas V, Maj G (2018) Towards real-time optical measurement of microbubble content in hydrodynamic test facilities. In: 10th Int Symp on Cavitation (CAV2018), Baltimore, Maryland, USA, pp 1056–1061

Russell P, Venning J, Pearce B, Brandner P (2020a) Calibration of Mie Scattering Imaging for microbubble measurement in hydrodynamic test facilities. Experiments in Fluids 61(4):1–17

Russell PS, Barbaca L, Venning JA, Pearce BW, Brandner PA (2020b) Measurement of nuclei seeding in hydrodynamic test facilities. Exp Fluids 61(3):1–18

Testa C, Ianniello S, Salvatore F (2018) A Ffowcs Williams and Hawkings formulation for hydroacoustic analysis of propeller sheet cavitation. J Sound and Vibration 413:421–441

Welch P (1967) The use of fast fourier transform for the estimation of power spectra: a method based on time averaging over short, modified periodograms. IEEE Trans on audio and electroacoustics 15(2):70–73